Available online at www.sciencedirect.com
ScienceDirect
Trans. Nonferrous Met. Soc. China 31(2021) 2999−3011
Transactions of Nonferrous Metals Society of China
www.tnmsc.cn

Influence of microstructural characteristics on corrosion behavior of Mg–5Sn–3In alloy in Hank's solution

Xue-jian WANG[1], Zong-ning CHEN[1,2], Yu-bo ZHANG[3], En-yu GUO[1,2], Hui-jun KANG[1,2], Pei HAN[3], Tong-min WANG[1,2]

1. Key Laboratory of Solidification Control and Digital Preparation Technology (Liaoning Province), School of Materials Science and Engineering, Dalian University of Technology, Dalian 116024, China;
2. Ningbo Institute of Dalian University of Technology, Ningbo 315000, China;
3. Orthopaedic Department, Shanghai Jiao Tong University Affiliated Sixth People's Hospital, Shanghai 200233, China

Received 27 September 2020; accepted 20 June 2021

Abstract: The microstructural observation, the mass loss test, potentiodynamic polarization measurements and corrosion morphology examinations were conducted to study the influence of microstructural characteristics on corrosion behavior of Mg–5Sn–3In alloys in Hank's solution after extrusion. The results show that the corrosion rate of the as-cast alloy is similar to that of as-extruded alloy; however, the local corrosion susceptibility is greatly weakened in the as-extruded alloy, especially in the extrusion direction. The relatively uniform corrosion morphology of the as-extruded alloy is attributed to refined Mg_2Sn particles, uniform distribution of Mg_2Sn particles and favorable crystal orientation. Meanwhile, the cytotoxicity tests confirm that the Mg–5Sn–3In alloy exhibits cytotoxicity of Grade 0−1 for NIH3T3 cells, suggesting an acceptable cytotoxicity of this alloy in the vitro assay.
Key words: Mg–Sn alloy; indium element; microstructure; corrosion behavior; cytotoxicity

1 Introduction

Magnesium is non-toxic and nutrient element in the human body, and is beneficial to many metabolic reactions and biological functions [1,2]. Moreover, the elastic modulus of magnesium and magnesium alloys is close to that of human femur bone, minimizing the "stress-shield" effect for human body [3]. These unique and intriguing characteristics have attracted considerable attention to developing magnesium alloys as biodegradable materials [4−6].

However, one of the major constraints in practical clinical applications for magnesium or/and its alloys is uncontrolled corrosion rate in aqueous solutions [1,7]. It is well known that alloying is an effective way to modify the magnesium degradation ability in biological environment [8,9]. Sn element has higher hydrogen evolution overpotential than magnesium, which can reduce the hydrogen evolution rate and thus improve corrosion resistance of magnesium alloys [10]. ZENGIN et al [11] reported that the corrosion resistance of AS21 alloy is gradually improved by Sn additions. In addition, Sn is nutrient and trace element in human body [12]. The Sn-deficient condition leads to poor growth of human body and reduces feeding efficiency in rat studies [8]. However, the excessive Sn element added to magnesium alloy usually results in the formation of large amount of Mg_2Sn phase. The Mg_2Sn phase is effective site to initiate pitting corrosion, because the electrochemical potential of Mg_2Sn phase is nobler than that of

Corresponding author: En-yu GUO, Tel: +86-411-84709500, Fax: +86-411-84706790, E-mail: eyguo@dlut.edu.cn;
Pei HAN, Tel: +86-18930173620, E-mail: hanpei_cn@163.com
DOI: 10.1016/S1003-6326(21)65709-6

magnesium matrix [13−15]. We found in the previous study [16] that the dissolved In element in α-Mg reduces the potential difference between the Mg_2Sn phase and α-Mg matrix, thereby decreasing the effect of Mg_2Sn as the cathodic phase for Mg−5Sn alloy in the 3.5 wt.% NaCl solution. Therefore, the Mg−Sn−In alloy system was selected in this work to further study the corrosion behavior of the alloy in Hank's solution.

Mechanical processing such as rolling, hot extrusion and equal channel angular pressing have been reported to modify the microstructure of Mg alloys and thus to alter the corrosion behavior [17,18]. SONG et al [19] found that the AZ91D magnesium alloy displayed a significantly higher corrosion rate with increasing pass of equal channel angular pressing, forming more pits in NaCl solution. Therefore, the influence of mechanical work on the biodegradation behavior of Mg−Sn alloys remains a question that needs to be studied.

In this work, the Mg−5Sn−3In alloy was selected as the studied material. This alloy was cast initially and then subjected to hot extrusion. We aimed to reveal the impact of microstructure modification, caused by extrusion, on corrosion behavior of this alloy, and thus uncovering the corrosion mechanism. Mass loss tests, electrochemical tests and corrosion morphology observations were conducted to evaluate the corrosion rate with different processing conditions. Finally, the cytotoxicity of Mg−5Sn−3In alloy was evaluated in vitro.

2 Experimental

2.1 Materials and microstructure characterization

Mg−5Sn−3In alloy ingot with nominal composition of 5 wt.% Sn and 3 wt.% In was prepared by melting high purity Mg (99.99%), Sn (99.99%) and In (99.995%) in a magnesia crucible under protection of a mixed gas atmosphere of SF_6 and CO_2 in a resistance furnace. The melt was cast into a preheated steel mould at 523 K with a diameter of 70 mm. The as-cast ingot was treated with solid solution at 723 K for 24 h followed by water cooling. The sample with a diameter of 60 mm and height of 30 mm after solution was extruded into a square bar with a square section area of 12 mm × 12 mm at the speed of 13 mm/s. The extrusion was performed at the temperature of 573 K and the extrusion ratio was set to be 20:1.

The microstructures and corrosion properties of the as-cast Mg−5Sn−3In alloy (denoted as as-cast-TI53), as well as extruded alloy in the parallel extrusion direction (denoted as ED-TI53) and perpendicular to extrusion direction (denoted as TD-TI53) were evaluated and compared. The extracted positions of ED-TI53 and TD-TI53 from the extruded bar are shown Fig. 1. The dimensions of samples for microstructure, immersion test and electrochemical test were 12 mm × 12 mm × 2 mm. The microstructure of samples was analyzed using an electron probe micro-analyzer (EPMA, JXA−8530F Plus) that was operated in a back scattered electron imaging mode. The transmission electron microscope (TEM, JEOL JEM−2100F) was used to further characterize the detailed microstructure. The phases were measured by an X-ray diffractometer (XRD, PANalytical Empyrean) with Cu K_α radiation at a scanning speed of 0.14 (°)/s.

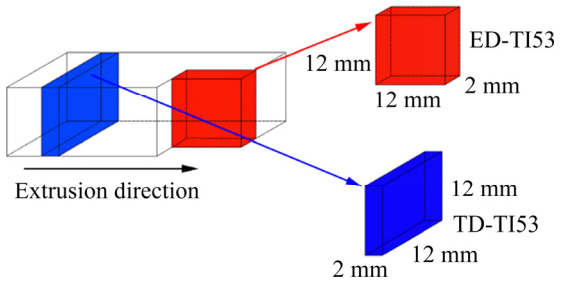

Fig. 1 Extracted positions of ED-TI53 and TD-TI53 from extruded bar

2.2 Immersion and electrochemical tests

The samples for immersion test were mechanically ground with SiC papers up to 2000 grit. Then, each sample was immersed in 250 mL Hank's solution up to 20 d at (37±0.5) °C. The Hank's solution was replaced by a fresh one every 7 d. The chemical composition of Hank's simulation body fluids is listed in Table 1. Corrosion products were removed using 200 g/L CrO_3+10 g/L $AgNO_3$ solution for 8 min. Surface morphology of corroded samples was observed by scanning electron microscope (SEM, Zeiss supra 55, Zeiss Corp) fitted with an energy dispersive spectroscopy (EDS). Corrosion rate was calculated according to ASTM standard G31—72(2004) [20]:

$$P=KW/(At\rho) \quad (1)$$

Table 1 Chemical composition of Hank's solution at pH of 7.4±0.2 (g/L)

NaCl	KCl	$CaCl_2$	$NaHCO_3$	KH_2PO_4	$C_6H_{12}O_6$	$Na_2HPO_4·12H_2O$	$MgCl_2·6H_2O$	$MgSO_4·7H_2O$
8.00	0.40	0.14	0.35	0.06	1.00	0.06	0.10	0.06

where P is the corrosion rate in mm/a, K is a constant (8.76×10^4), W is the mass loss of sample in g, A is the surface area of sample in cm^2, t is the immersion time in h, and ρ is the density in g/cm^3. For each condition, at least three samples were tested to obtain good statistics.

Before electrochemical test, the samples were ground with SiC papers up to 2000 grit, washed with distilled water, and dried by cold air. A conventional three-electrode system consisting of a platinum foil as the counter electrode, a Ag/AgCl electrode as the reference electrode and the sample (0.7854 cm^2 for exposed area) as the working electrode was employed to obtain electrochemical parameters at (37±0.5) °C. The potentiodynamic polarization test was measured at a scanning rate of 0.5 mV/s. Polarization curves were fitted using Tafel extrapolation method. Corrosion rate was calculated by [21]

$$P=\frac{3270J_{\text{corr}}}{\rho V}M \tag{2}$$

where J_{corr} is the corrosion current density in A/cm^2, M is the relative molecular mass in g, and V is the valence number (electrons lost during the oxidation reaction). At least three samples were tested for each sample condition to ensure the accuracy.

2.3 Cytotoxicity test

Cell viability was conducted by indirect method with the NIH3T3 cells according to the International Organization for Standardization (ISO 10993—5) [22]. The NIH3T3 cells were cultured in Dulbecco's modified eagle's medium (DMEM, Hyclone, Logan, USA), supplied with 10% fetal bovine serum (FBS, Invitrogen, Carlsbad, USA), 2 mmol/L glutamine, 100 U/mL penicillin and 100 μg/mg streptomycin in a humidified atmosphere of 5% CO_2 at 37 °C. The extracts of studied alloys were prepared by DMEM and incubated for 24 h with an extraction ratio of 1.25 cm^2/mL. The cell viability was assessed using CCK-8 assays. NIH3T3 cells were seeded at a density of 5×10^3 cells/mL in the 96-well tissue culture plate and cultured with complete DMEM in a humidified incubator containing 5% CO_2 at 37 °C. After 24 h, the culture medium was replaced by the extracts and kept further incubation for 1, 3 and 5 d, respectively. The cell culture medium was adopted as negative control. At determined time, the extracts of each well were replaced by a mixture of 10 μL Kit-8 (CCK-8, Donjindo, Kumamoto, Japan) and 90 μL culture medium and incubated for 2 h. The spectrophotometrical absorbance of each well was measured by a microplate reader (BioTek, Winooski, VT, USA) at a wavelength of 450 nm. Three duplicates of each group were adopted for cell viability assay.

3 Results and discussion

3.1 Microstructures

Figure 2(a) shows backscattered electron microscope image of as-cast-TI53 alloy. The microstructure of as-cast-TI53 alloy exhibits typical dendritic morphology. In our previous study [18], the as-cast Mg−5Sn−3In alloy is composed of α-Mg matrix, Mg_2Sn phase and element enriched areas. In element is mainly enriched in interdendritic areas and dissolved in α-Mg matrix. However, it is clearly observed in Figs. 2(b) and (c) that element enriched areas are eliminated after extrusion. The Mg_2Sn particles are both precipitated within the grains and grain boundaries. Figure 2(d) shows the bright field TEM image of Mg_2Sn particles in as-cast-TI53 alloy. It is seen that the Mg_2Sn particles are in micron scale size. Compared to as-cast-TI53 alloy, the spherical Mg_2Sn particles with nanometer and sub-micron scales are observed in ED-TI53 alloy, as shown in Fig. 2(e). Spherical Mg_2Sn particles with different length scales are usually found in hot deformed Mg−Sn based alloys [23,24]. Figures 2(f) and (g) show the (0001) and $(10\bar{1}0)$ pole figures of ED-TI53 alloy, respectively. It is apparent that ED-TI53 alloy exhibits a typical basal texture, as indicated by the maximum intensity of basal texture of 12.8.

The size and morphology of Mg_2Sn particles are changed, but also the distribution and area fraction of Mg_2Sn particles have varied in different conditions. The area fraction of Mg_2Sn particles in ED-TI53 and TD-TI53 alloys is higher than that in

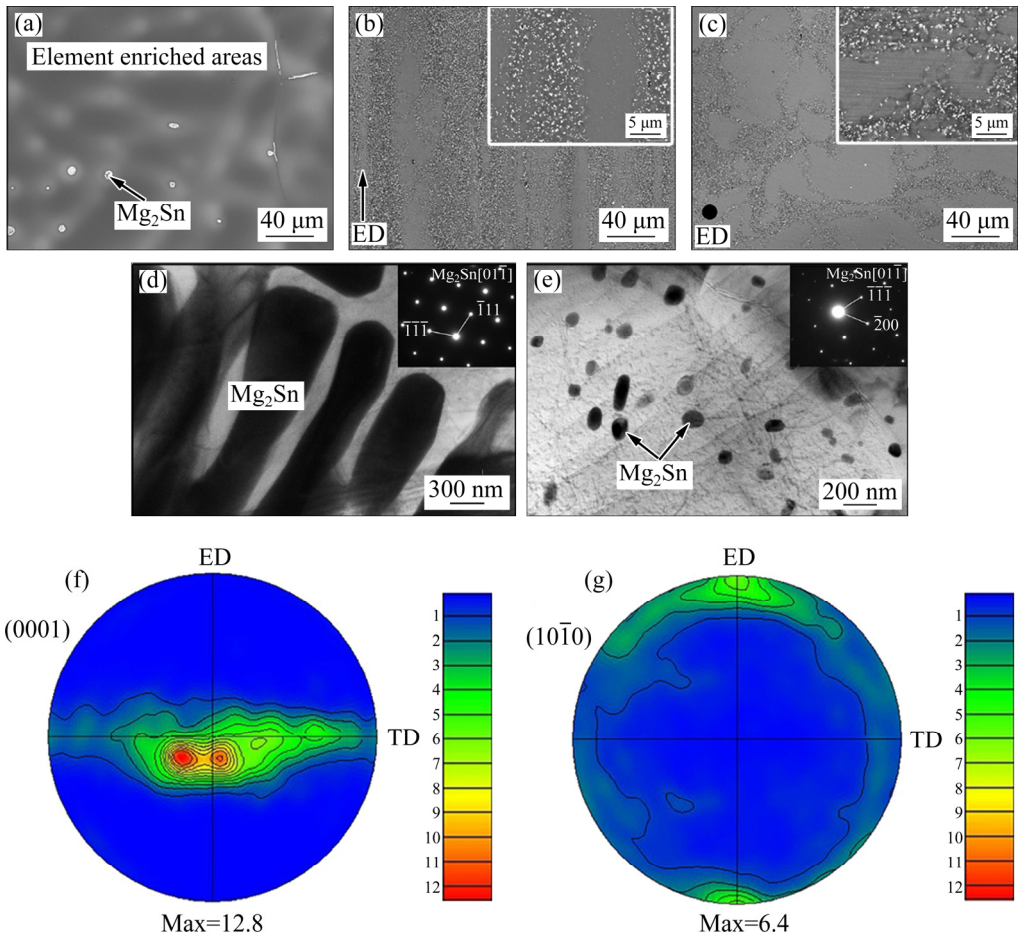

Fig. 2 Backscattered electron microscope images of as-cast-TI53 (a), ED-TI53 (b), and TD-TI53 (c) alloys (the inset in each figure shows magnified image of the local area), TEM image and SAED pattern of Mg_2Sn particles in as-cast-TI53 (d) and ED-TI53 alloys (e), and pole figures of (0001) (f) and $(10\bar{1}0)$ (g) for ED-TI53 alloy

the as-cast-TI53 alloy. The reasons are summarized as follows: (1) the maximum solid solubility of Sn in Mg, 14.85 wt.% at 561.2 °C, drastically declines to 0.45 wt.% at 200 °C, resulting in the precipitation of Mg_2Sn particles with the decreasing temperature [25]; (2) no Sn element enriched areas are present in ED-TI53 and TD-TI53 alloys, resulting in a high content of Sn to precipitate and form Mg_2Sn particles; (3) the dynamic precipitation of Mg_2Sn can be enhanced by the mechanical straining arising during extrusion processing; (4) the intermetallic particles increase more significantly on the (0001) plane than those on $(10\bar{1}0)$ plane after heat treatment [26].

Figure 3 shows the element distribution of TD-TI53 alloy. The Sn element enriches in the bright Mg_2Sn phase, while In element is evenly distributed in α-Mg matrix. This is because the In element has a high solid solubility (53.2 wt.%) in Mg. Thus, In element is mostly dissolved in α-Mg matrix for the extruded Mg−5Sn−3In alloy. Figure 4 shows the results of XRD measurements. It can be seen that the intensity of Mg_2Sn diffraction peaks in ED-TI53 and TD-TI53 alloys is higher than that in the as-cast-TI53 alloy, suggesting that the volume fraction of Mg_2Sn particles is higher in the extruded alloy. No other phases except Mg and Mg_2Sn are detected in the XRD measurements.

3.2 Corrosion properties

Figure 5 shows that the average corrosion rate is calculated by the mass loss rate after 20 d immersion in Hank's solution. The corrosion rates are (0.489±0.080), (0.422±0.049) and (0.494±0.041) mm/a for as-cast-TI53, ED-TI53 and TD-TI53 alloys, respectively. The difference of corrosion rate is minor, and ED-TI53 alloy exhibits relatively optimal corrosion resistance. Figure 6 shows potentiodynamic polarization curves of the studied alloys after immersion for 0 and 3 d,

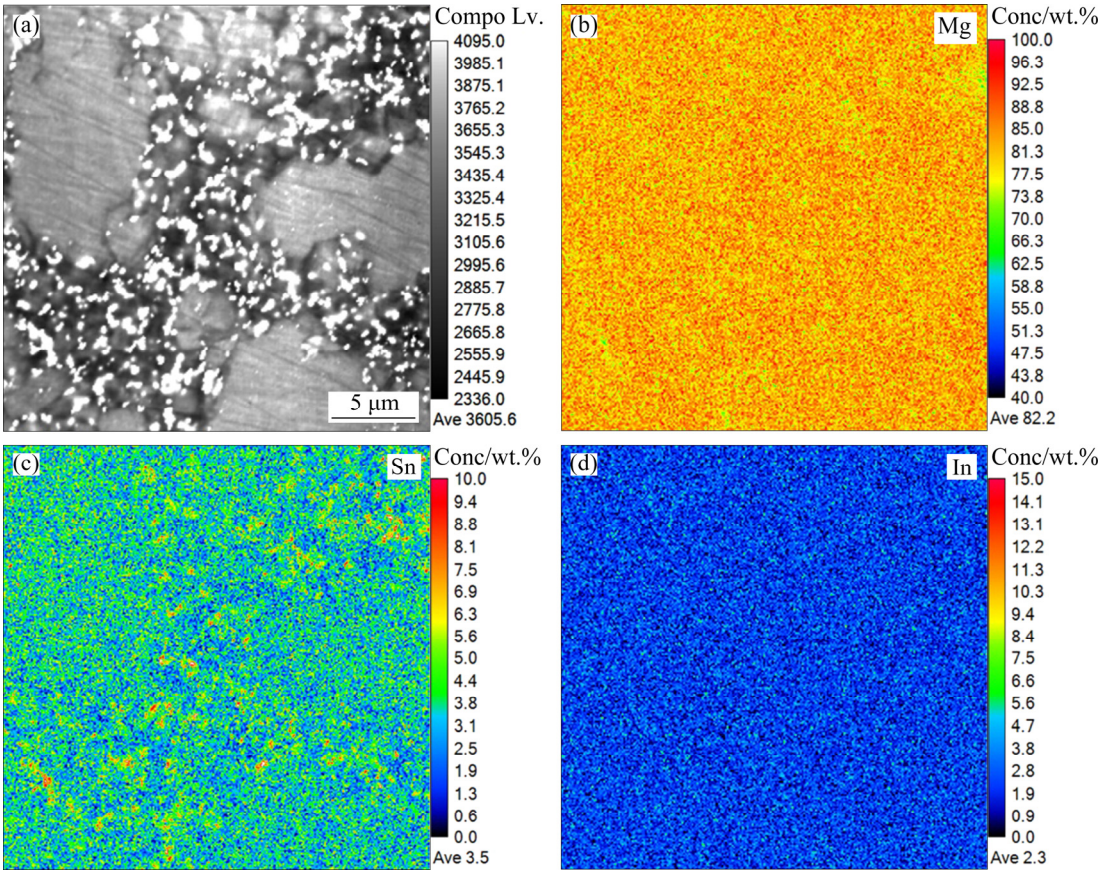

Fig. 3 Backscattered electron microscope image of TD-TI53 alloy (a), and element distribution in TD-TI53 alloy of Mg (b), Sn (c) and In (d)

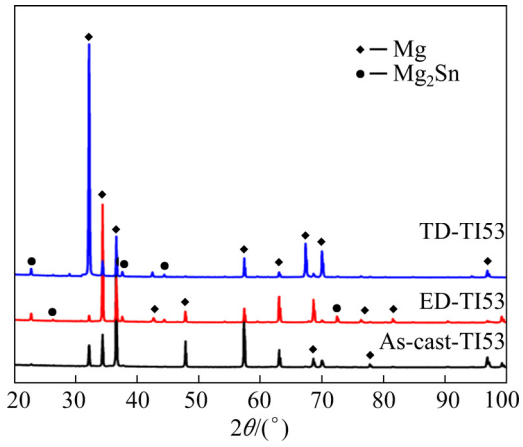

Fig. 4 XRD patterns of as-cast-TI53, ED-TI53 and TD-TI53 alloys

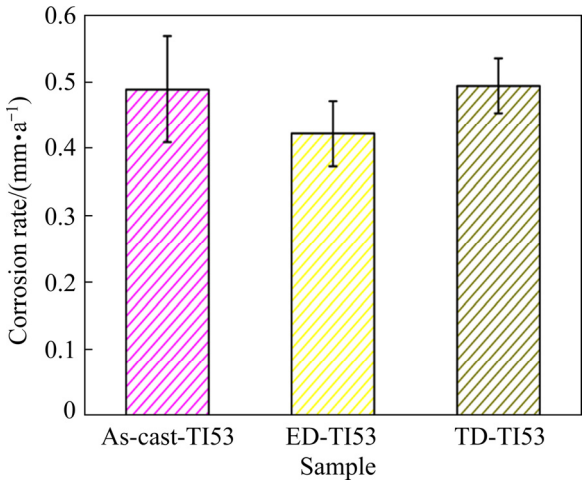

Fig. 5 Average corrosion rates of as-cast-TI53, ED-TI53 and TD-TI53 alloys in Hank's solution for 20 d

respectively. The corrosion current density (J_{corr}) is obtained using Tafel extrapolation method to fit the potential range from −130 mV (vs corrosion potential (φ_{corr})) to −100 mV (vs φ_{corr} on cathodic branch). The φ_{corr}, J_{corr} and the average corrosion rate (P_i) obtained from the potentiodynamic polarization curves are summarized in Table 2.

It can be found in Fig. 6(a) that the as-cast-TI53 alloy shows the lowest J_{corr} after immersion for 0 d, which is not consistent with the corrosion rates obtained by mass loss method. Corrosion process of magnesium alloys generally occurs via anodic reaction of Mg dissolution and cathodic reaction of hydrogen evolution [27]. The reactions can be described by

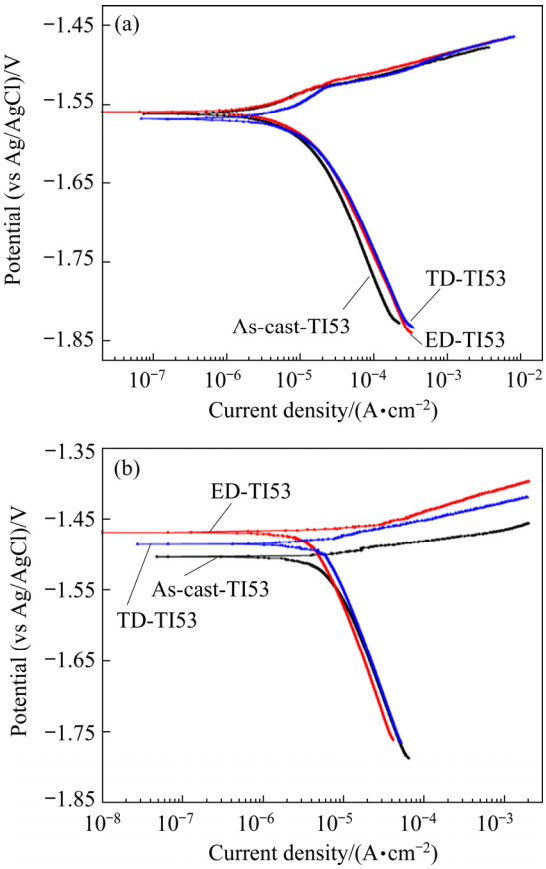

Fig. 6 Potentiodynamic polarization curves of as-cast-TI53, ED-TI53 and TD-TI53 alloys after immersion for 0 d (a) and 3 d (b)

Table 2 Fitting results derived from potentiodynamic polarization curves

Immersion time/d	Alloy	φ_{corr}(vs Ag/AgCl)/V	J_{corr}/(μA·cm^{-2})	P/(mm·a^{-1})
0	As-cast-TI53	−1.562	13.93	0.318
	ED-TI53	−1.559	15.62	0.357
	TD-TI53	−1.569	18.80	0.430
3	As-cast-TI53	−1.504	8.24	0.188
	ED-TI53	−1.469	5.33	0.122
	TD-TI53	−1.486	7.88	0.180

Anodic reaction: $Mg \rightarrow Mg^{2+}+2e$ (3)

Cathodic reaction: $2H_2O+2e \rightarrow H_2+2OH^-$ (4)

In the Mg−Sn alloys, Mg_2Sn particles act as the cathodic phase in corrosion process. The distribution and quantity of Mg_2Sn particles are quite different in the studied alloys, which have remarkable influence on cathodic polarization. The cathodic current density increases in ED-TI53 and TD-TI53 alloys due to the increase in area fraction of Mg_2Sn particles. SONG and ATRENS [27] reported that the discrete distribution of $Mg_{17}Al_{12}$ phase can deteriorate corrosion resistance of alloy after extrusion. Meanwhile, GUI et al [28] found that reducing volume fraction of the $(MgZn)_3Gd$ particles may increase the corrosion resistance of the extruded Mg−3.0Gd−2.7Zn−0.4Zr−0.1Mn alloy. Thus, the corrosion rates of ED-TI53 and TD-TI53 alloys are enhanced with the increasing secondary phases in the early stage of the corrosion.

However, the dissolved In element in α-Mg reduces the potential difference between the Mg_2Sn phase and α-Mg matrix, thereby decreasing the effect of Mg_2Sn as the cathodic phase [16]. Most of In is dissolved in α-Mg matrix for ED-TI53 and TD-TI53 alloys due to the solution treatment before extrusion. Thus, ED-TI53 and TD-TI53 alloys exhibit higher corrosion resistance than as-cast-TI53 alloy. In addition, the grain sizes of the as-cast and extruded Mg–5Sn–3In alloys are (290.1±20.6) and (1.96±0.14) μm, respectively. ED-TI53 and TD-TI53 alloys have more grain boundaries than as-cast-TI53 alloy due to refined grains. The boundaries of grains and α-Mg are high activity areas, and thus the corrosion reaction mainly occurs in high activity area of α-Mg matrix and grain boundaries. The protective oxidation film and corrosion products are formed on α-Mg matrix and at the grain boundaries. In order to indicate the effect of protective oxidation film and corrosion products on corrosion process, the potentiodynamic polarizations after immersion for 3 d are performed. Compared to the curves after immersion for 0 d, the enhancement of φ_{corr} after immersion for 3 d indicates that the partially protective oxidation film on the surface of Mg−5Sn−3In alloy hinders the corrosion reaction in terms of thermodynamics. The J_{corr} obtained from the potentiodynamic polarizations after immersion for 3 d indicates that the formed films of ED-TI53 and TD-TI53 are advantageous over those of as-cast-TI53 alloy for protecting the matrix. This is because the refined grains are beneficial to a more rapid formation of a protective layer on the surface of alloys due to increasing reactivity sites for the nucleation of oxide film [28,29].

3.3 Corrosion morphology

Figures 7(a−c) show corrosion morphologies

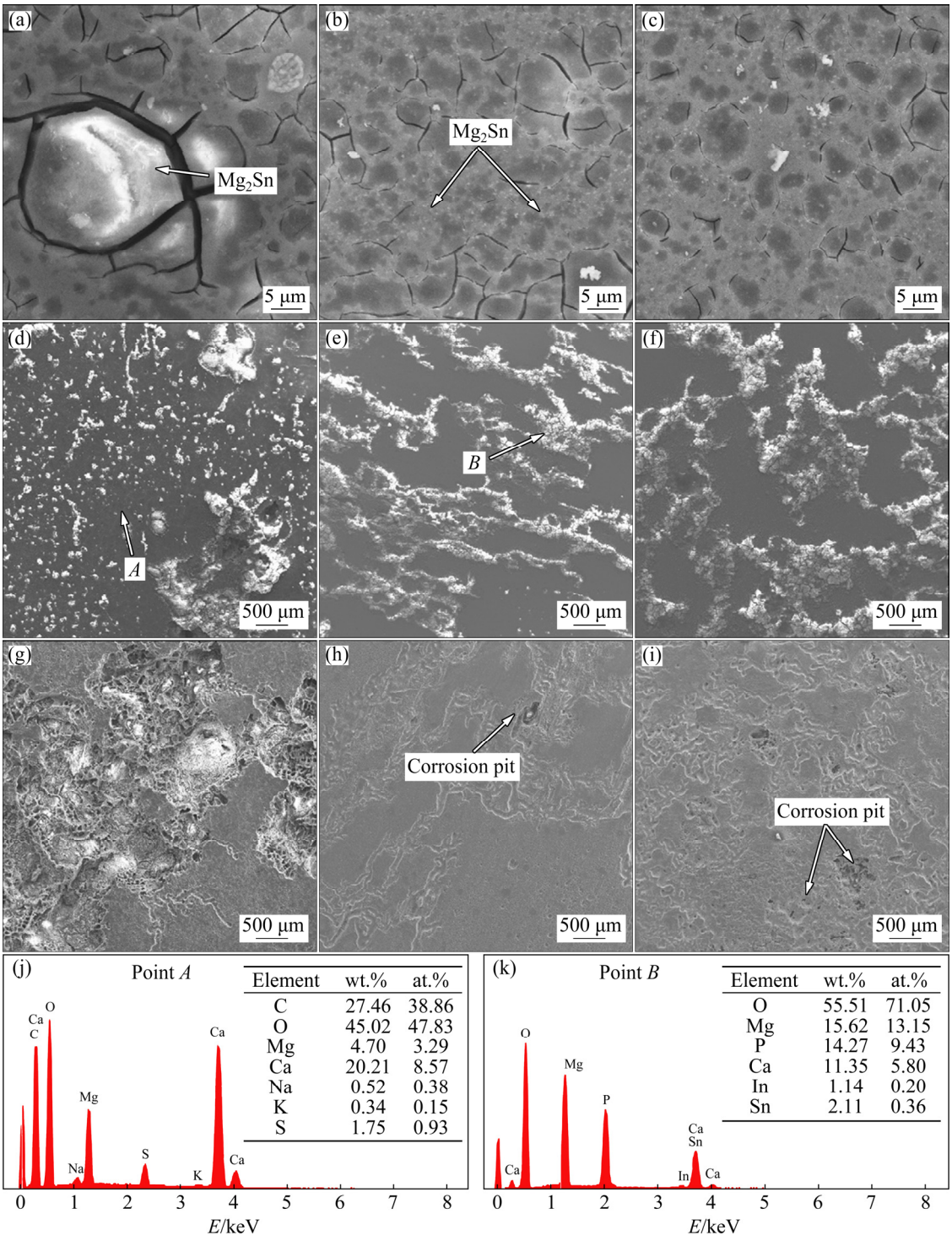

Fig. 7 Corrosion morphologies of as-cast-TI53 (a), ED-TI53 (b) and TD-TI53 (c) alloys after 1 d immersion in Hank's solution, corrosion morphologies of as-cast-TI53 (d), ED-TI53 (e) and TD-TI53 (f) alloys after 7 d immersion in Hank's solution, surface morphologies of as-cast-TI53 (g), ED-TI53 (h) and TD-TI53 (i) alloys after removing corrosion products and 20 d immersion in Hank's solution, and EDS results at selected Points *A* (j) and *B* (k)

of the studied alloys after immersion in Hank's solution for 1 d. It is seen that corrosion is initiated around the Mg_2Sn particles. Coarse Mg_2Sn particles are corroded seriously as compared with fine Mg_2Sn particle in as-cast-TI53 alloy. The small and intact Mg_2Sn particles are found in ED-TI53 and TD-TI53 alloys. The cracks of corrosion film are formed due to dehydration in air for all the alloys.

Figures 7(d−f) show the corrosion morphologies of the studied alloys after immersion in Hank's solution for 7 d. The surfaces of all the alloys are covered by corrosion film and white corrosion products. Spherical corrosion products and a large corrosion pit are found on as-cast-TI53 alloy surface, as shown in Fig. 7(d). In comparison, the corrosion products present strip distribution and no corrosion pits are found on the surfaces of ED-TI53 and TD-TI53 alloys. Therefore, the distribution of corrosion products is dominated by the distribution of Mg_2Sn particles. Figures 7(g−i) show the surface morphologies of as-cast-TI53, ED-TI53 and TD-TI53 alloys after 20 d immersion in Hank's solution. The corrosion products were removed to show the morphology. It is seen that the surface of as-cast-TI53 alloy is ruptured in most of the regions and sever local corrosion occurs. The ED-TI53 and TD-TI53 alloys exhibit filiform corrosion morphology and contain a number of deep pits. The results demonstrate that corrosion morphology varies depending on the structures [30,31]. The fine and uniform Mg_2Sn particles can greatly hinder corrosion pits to expand in depth direction. Thus, the corrosion damage level of the extruded alloy after immersion for 20 d in Hank's solution is much weaker than that of the as-cast alloy. The EDS analysis of Points *A* and *B* shows that corrosion products mainly contain O, C, Mg, Ca and P elements. In Hank's solution, aside from the magnesium oxide and magnesium hydroxides, (Ca,Mg) carbonates and (Ca,Mg) phosphates are usually found to be the main components of the corrosion products which are partly protective [32,33].

Figure 8 shows the back-scattered electron images of the cross-section of alloys after immersion in Hank's solution for 20 d. Figure 8(a) shows that a typical local corrosion morphology is present in as-cast-TI53 alloy, and the remarkable corrosion depth is measured to be 192.5 μm. The magnified morphology in Fig. 8(b) shows that the

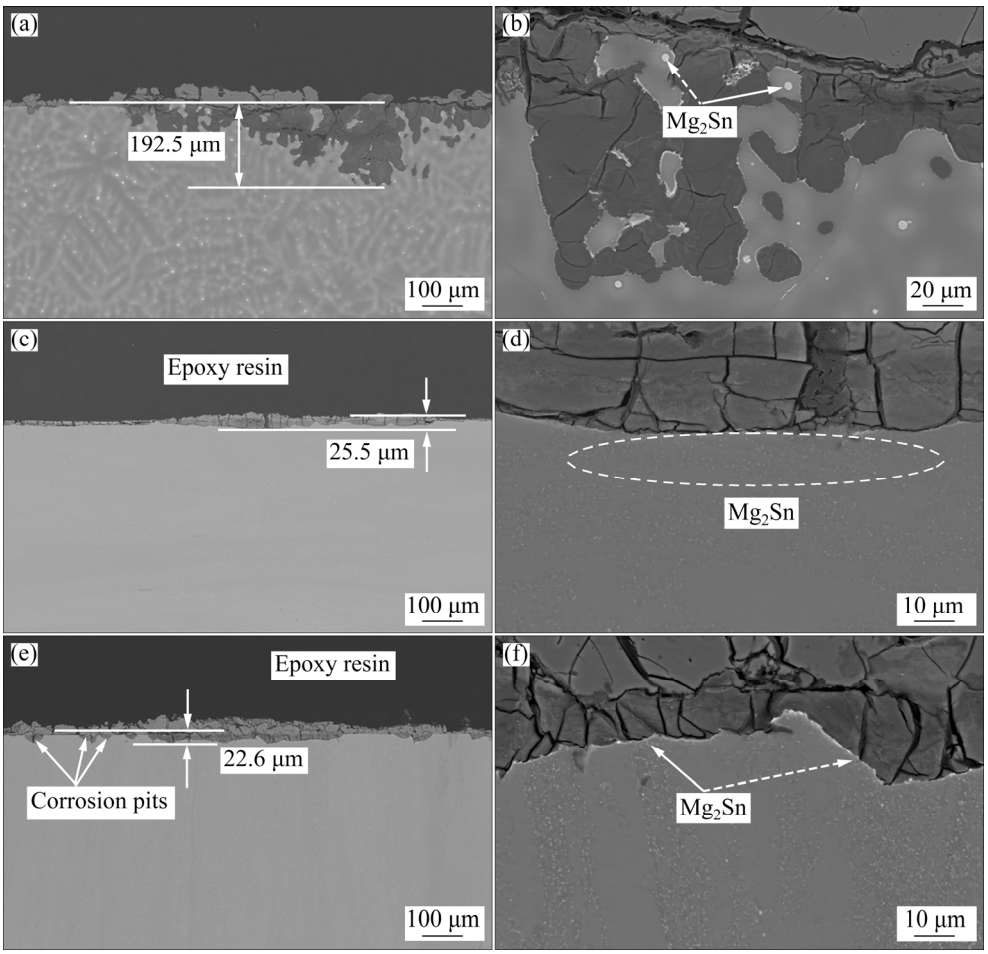

Fig. 8 BSE images of cross-section of alloys after 20 d immersion in Hank's solution: (a, b) As-cast-TI53; (c, d) ED-TI53; (e, f) TD-TI53 ((b, d, f) present the magnified local corrosion regions of as-cast-TI53, ED-TI53 and TD-TI53, respectively)

α-Mg matrix adjacent to interdendritic areas is corroded seriously, and the interdendritic areas are slightly attacked. Figures 8(c) and (e) show that the local corrosion is alleviated after extrusion, and the maximum local corrosion depth of TD-TI53 alloy is reduced to only 22.6 μm. However, corrosion depth of ED-TI53 alloy is more uniform than that of TD-TI53 alloy. Some separate corrosion pits are observed in TD-TI53 alloy. Studies have revealed that crystallographic feature affects the initiation and propagation of the localized attacks [34−36]. For example, the magnesium $(10\bar{1}0)$ and $(11\bar{2}0)$ planes can easily initiate pitting corrosion at small potentials over the corrosion potential, while magnesium (0001) plane alleviates the pitting corrosion susceptibility [37]. ED-TI53 alloy exhibits a typical basal texture, as shown in Fig. 2(f), and thus the strong basal texture inhibits the initiation of pitting corrosion. In addition, the distribution of Mg_2Sn particles is more uniform in ED-TI53 alloy than that in TD-TI53 alloy, slowing down corrosion process beneath corrosion products, as shown in Figs. 8(d) and (f). Thus, ED-TI53 alloy possesses the lower tendency for pits growth and lower dissolution rate in Hank's solution, due to the strong basal texture and more uniform distribution of Mg_2Sn particles.

Figure 9 shows the corrosion mechanisms during the corrosion process of each sample. As shown in Fig. 9(a), in Stage I, the micro-galvanic corrosion consists of anodic α-Mg matrix and cathodic Mg_2Sn particles. It has been reported that the rate of the micro-galvanic corrosion is primarily determined by the area ratio of anodic to cathodic phases and the difference of electrical potential between anodic and cathodic phases [38,39]. The Mg_2Sn particles in as-cast-TI53 alloy are much larger than those in ED-TI53 and TD-TI53 alloys. The coarse Mg_2Sn particles are easier to initiate pitting corrosion than the finer Mg_2Sn particles, as

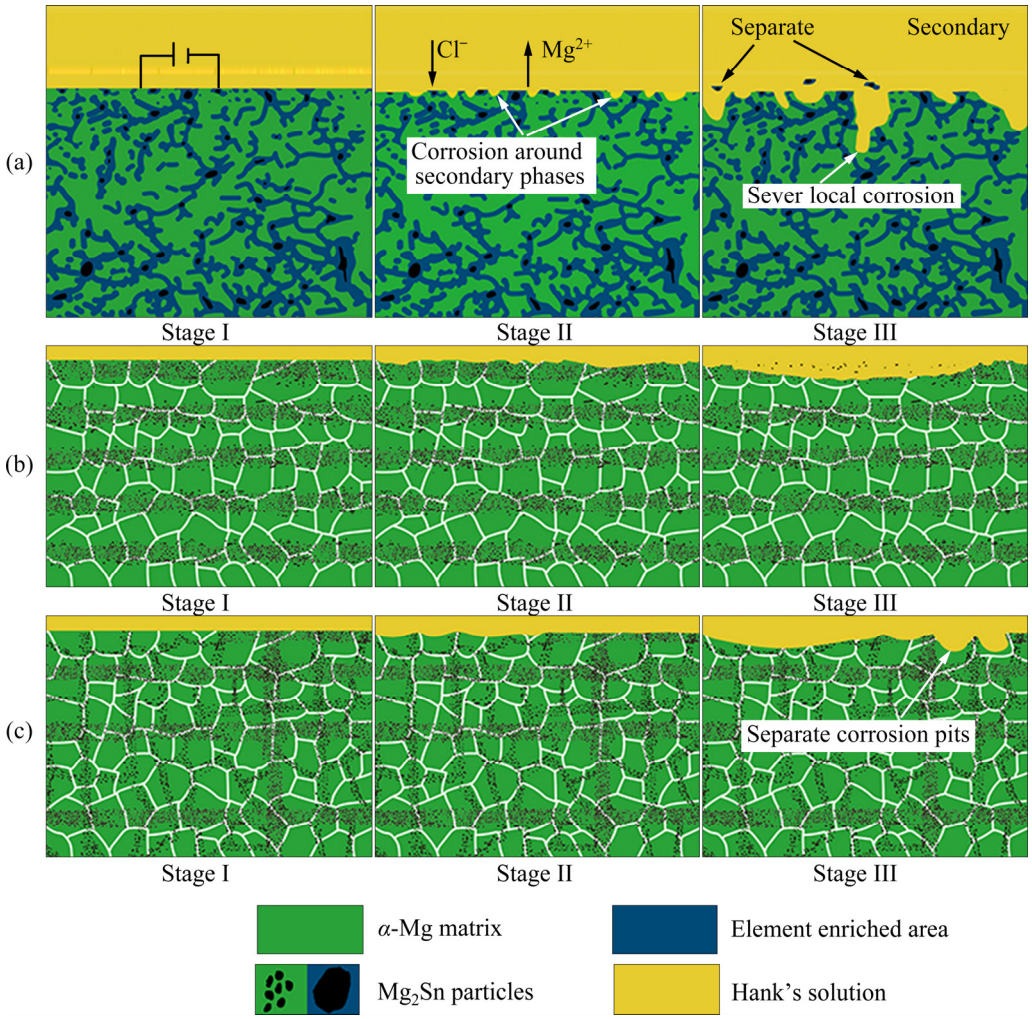

Fig. 9 Schematic diagrams of corrosion mechanism: (a) As-cast-TI53 alloy; (b) ED-TI53 alloy; (c) TD-TI53 alloy

shown in Fig. 7. Thus, the local micro-galvanic corrosion rate of ED-TI53 and TD-TI53 alloys is much lower.

In Stage II, oxides and hydroxides protective films formed in the corrosion initial stage are damaged in Cl^--containing solution as the immersion time increases. The α-Mg matrix is preferentially dissolved along the interdendritic areas as Mg_2Sn particles are distributed in interdendritic areas for as-cast-TI53 alloy. Once α-Mg matrix nearby the Mg_2Sn particles is completely dissolved, Mg_2Sn particles gradually peel off and corrosion cavities are formed. The bare metal contacts with Hank's solution, and the repassivation process is less likely to occur in the corrosion cavity. The corrosion cavity increases the roughness of the bare surface and further increases area ratio of cathodic to anodic to accelerate the corrosion rate. The interdendritic areas are more corrosion resistant than α-Mg matrix. Therefore, corrosion develops into the interior part of as-cast-TI53 alloy, and promotes the separation of interdendritic areas from matrix. However, after the protective film breaks, fine Mg_2Sn particles provide more homogeneous sites for pitting corrosion to occur in ED-TI53 and TD-TI53 alloys. The fine Mg_2Sn particles with uniform distribution make each pit difficult to grow, as shown in Figs. 9(b) and (c).

In Stage III, the local corrosion becomes more serious in as-cast-TI53 alloy, while a large number of fine Mg_2Sn particles peel off and small corrosion pits merge in ED-TI53 and TD-TI53 alloys. However, it is found in Figs. 7 and 8 that the corrosion morphologies of ED-TI53 and TD-TI53 alloys are quite different. Compared with ED-TI53 alloy, the Mg_2Sn particles with net-like distribution in TD-TI53 alloy cause the increasing exposed area of α-Mg matrix, thus accelerating corrosion rate. The separate corrosion pits are finally formed inside net-like distributed Mg_2Sn particles.

3.4 Cytotoxicity

Figure 10 shows the changes of optical density (OD) values and cell viabilities with varying incubation time. After 1 d of incubation, the difference of the OD value is small between as-cast-TI53 and ED-TI53 alloys, whereas both of them are higher than that of TD-TI53 alloy. Except for ED-TI53 alloy, the OD values increase with the increase of incubation time up to 3 d. The decreasing OD value of ED-TI53 alloy after 5 d may be due to exfoliation of many Mg_2Sn particles. The OD values of all the alloys are higher than that of control group, suggesting that the extracts promote the cell proliferation. The variations of cell viability values are shown in Fig. 10(b). It is found that cell viability decreases slightly with the increase of incubation time. The deterioration on cell viability suggests lagged response of NIH3T3 and alkalinity circumstance due to the degradation of Mg−5Sn−3In alloy [40,41]. The result shows that all the cell viability values are more than 100% in all incubation time. According to ISO10993—5 [22], the cell viability values of as-cast-TI53, ED-TI53 and TD-TI53 ((123±7.2)%, (117±7.8)% and (128±12.8)%, respectively) after incubation for 5 d show the cytotoxicity of Grade 0−1, suggesting good cytotoxicity of these alloys. The alloys show similar cell viability because of the same chemical elements, contents and similar corrosion rates.

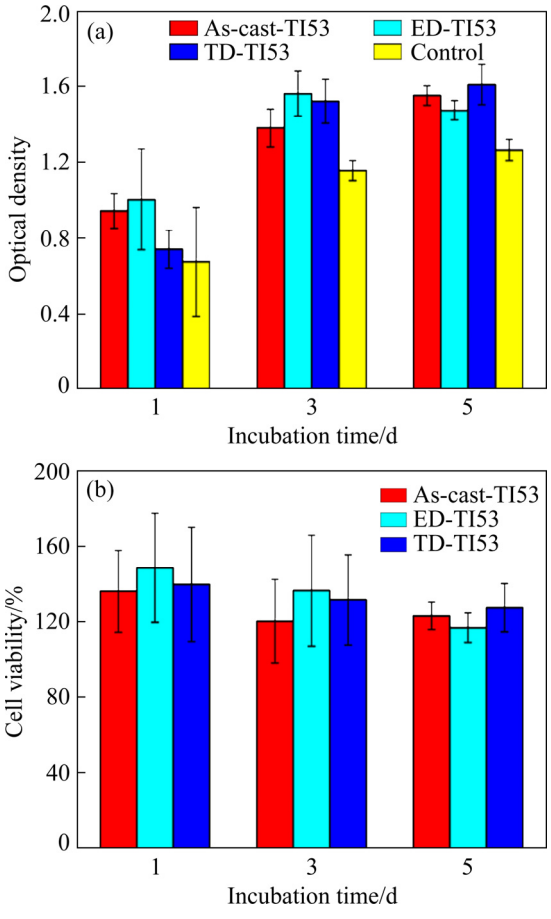

Fig. 10 Optical density of Mg–5Sn–3In samples (a) and cell viability of NIH3T3 (b) after incubation for 1, 3 and 5 d

4 Conclusions

(1) Interdendritic element enriched areas in as-cast alloy are eliminated, and In element is completely dissolved in α-Mg matrix after hot extrusion. The number and area fraction of Mg_2Sn particles are increased while the size of Mg_2Sn particles is reduced after extrusion.

(2) The area ratio of cathode to anode increases due to the increasing fraction of Mg_2Sn particles in the extruded alloy, leading to the increase of corrosion rate. However, the refine grain of the extruded alloy is beneficial to a more rapid formation of a protective layer on the surface of alloys, and thus improving the corrosion resistance. ED-TI53 alloy exhibits the optimum corrosion resistance in the three sample conditions.

(3) Mg_2Sn particles provide the initiative corrosion sites, and thus, the corrosion morphology is dependent on the distribution of Mg_2Sn particles. Local corrosion susceptibility is greatly weakened in ED-TI53 alloy because of the uniform distribution of fine Mg_2Sn particles and higher basal texture.

(4) The cytotoxicity experiments reveal that Mg−5Sn−3In alloy exhibits the cytotoxicity of Grade 0−1, suggesting an acceptable cytotoxicity of this alloy in the vitro assay.

Acknowledgments

The authors are grateful for the financial supports from the National Key Research and Development Program of China (No. 2017YFA0403803), the National Natural Science Foundation of China (Nos. 52022017, 51974058, 51525401, 51927801, 81974325), the Science and Technology Commission of Shanghai Municipality, China (No. 18ZR1428700), and the Liaoning Revitalization Talents Program, China (No. XLYC1808005).

References

[1] DU Wen-bo, LIU Ke, MA Ke, WANG Zhao-hui, LI Shu-bo. Effects of trace Ca/Sn addition on corrosion behaviors of biodegradable Mg−4Zn−0.2Mn alloy [J]. Journal of Magnesium and Alloys, 2018, 6: 1−14.

[2] BAKHSHESHI-RAD H R, DAYAGHI E, ISMAIL A F, AZIZ M, AKHAVAN-FARID A, CHEN X B. Synthesis and in-vitro characterization of biodegradable porous magnesium-based scaffolds containing silver for bone tissue engineering [J]. Transactions of Nonferrous Metals Society of China, 2019, 29: 984−996.

[3] AGARWAL S, CURTIN J, DUFFY B, JAISWAL S. Biodegradable magnesium alloys for orthopaedic applications: A review on corrosion, biocompatibility and surface modifications [J]. Materials Science & Engineering C, 2016, 68: 948−963.

[4] HAN Pei, CHENG Peng-fei, ZHANG Shao-xiang, ZHAO Chang-li, NI Jia-hua. In vitro and in vivo studies on the degradation of high-purity Mg (99.99 wt.%) screw with femoral intercondylar fractured rabbit model [J]. Biomaterials, 2015, 64: 57−69.

[5] LIU Bao-sheng, CAO Miao-miao, ZHANG Yue-zhong, HU Yong, GONG Chang-wei, HOU Li-feng, WEI Ying-hui. Microstructure, anticorrosion, biocompatibility and antibacterial activities of extruded Mg−Zn−Mn strengthened with Ca [J]. Transactions of Nonferrous Metals Society of China, 2021, 31: 358−370.

[6] WU Shu-xu, WANG Shou-ren, WANG Gao-qi, YU Xiu-chun, LIU Wen-tao, CHANG Zheng-qi, WEN Dao-sheng. Microstructure, mechanical and corrosion properties of magnesium alloy bone plate treated by high-energy shot peening [J]. Transactions of Nonferrous Metals Society of China, 2019, 29: 1641−1652.

[7] HOMAYUN B, AFSHAR A. Microstructure, mechanical properties, corrosion behavior and cytotoxicity of Mg−Zn−Al−Ca alloys as biodegradable materials [J]. Journal of Alloys and Compounds, 2014, 607: 1−10.

[8] ZHENG Yu-feng, GU Xuen-nan, WITTE F. Biodegradable metals [J]. Materials Science and Engineering R, 2014, 77: 1−34.

[9] NAM N D. Corrosion behavior of Mg−5Al based magnesium alloy with 1 wt.% Sn, Mn and Zn additions in 3.5 wt.% NaCl solution [J]. Journal of Magnesium and Alloys, 2014, 2: 190−195.

[10] KUBASEK J, VOJTECH D, LIPOV J, RUML T. Structure, mechanical properties, corrosion behavior and cytotoxicity of biodegradable Mg−X (X=Sn, Ga, In) alloys [J]. Materials Science and Engineering C, 2013, 33: 2421−2432.

[11] ZENGIN H, TUREN Y, AHLATCI H, SUN Y, KARAOĞLANLI A C. Influence of Sn addition on microstructure and corrosion resistance of AS21 magnesium alloy [J]. Transactions of Nonferrous Metals Society of China, 2019, 29: 1413−1423.

[12] CHEN Yong-jun, XU Zhi-gang, SMITH C, SANKAR J. Recent advances on the development of magnesium alloys for biodegradable implants [J]. Acta Biomaterialia, 2014, 10: 4561−4573.

[13] ZHAO Chao-yong, PAN Fu-sheng, ZHAO Shuang, PAN Hu-cheng, SONG Kai, TANG Ai-tao. Preparation and characterization of as-extruded Mg−Sn alloys for orthopedic applications [J]. Materials & Design, 2015, 70: 60−67.

[14] LIU Xian-bin, SHAN Da-yong, SONG Ying-wei, CHEN Rong-shi, HAN En-hou. Influences of the quantity of Mg_2Sn phase on the corrosion behavior of Mg−7Sn magnesium alloy [J]. Electrochimica Acta, 2011, 56: 2582−2590.

[15] HA H Y, KANG J Y, YIM C D, YANG J, YOU B S. Role of hydrogen evolution rate in determining the corrosion rate of

extruded Mg−5Sn−(1−4wt.%)Zn alloys [J]. Corrosion Science, 2014, 89: 275−285.

[16] WANG Xue-jian, CHEN Zhong-ning, REN Jing, KANG Hui-jun, GUO En-yu, LI Jie-hua, WANG Tong-min. Corrosion behavior of as-cast Mg–5Sn based alloys with In additions in 3.5 wt.% NaCl solution [J]. Corrosion Science, 2020, 164: 108318.

[17] PRITHIVIRAJAN S, NARENDRANATH S, DESAI V. Analysing the combined effect of crystallographic orientation and grain refinement on mechanical properties and corrosion behaviour of ECAPed ZE41 Mg alloy [J]. Journal of Magnesium and Alloys, 2020, 8: 1128−1143.

[18] CHEN Jun-xiu, ZHU Xiang-ying, TAN Li-li, YANG Ke, SU Xu-ping. Effects of ECAP extrusion on the microstructure, mechanical properties and biodegradability of Mg−2Zn−*x*Gd−0.5Zr alloys [J]. Acta Metallurgica Sinica (English Letters), 2020, 34: 205−216.

[19] SONG D, MA A B, JIANG J H, LIN P H, YANG D H, FAN J F. Corrosion behaviour of bulk ultra-fine grained AZ91D magnesium alloy fabricated by equal-channel angular pressing [J]. Corrosion Science, 2011, 53: 362−373.

[20] ASTM Standards No. G30—1972. Standard practice for laboratory immersion corrosion testing of metals [S]. 2004.

[21] CHANG C H, HUANG T C, PENG C W, YEH T C, LU H I, HUNG W I, WENG C J, YANG T I, YEH J M. Novel anticorrosion coatings prepared from polyaniline/graphene composites [J]. Carbon, 2012, 50: 5044−5051.

[22] ISO 10993—5. Biological evaluation of medical devices—Part 5: Tests for in vitro cytotoxicity [S]. 2009.

[23] SHI Zhang-zhi, XU Jun-yi, YU Jing, LIU Xue-feng. Microstructure and mechanical properties of as-cast and as-hot-rolled novel Mg−*x*Sn−2.5Zn−2Al alloys (*x*=2, 4 wt.%) [J]. Materials Science and Engineering A, 2018, 712: 65−72.

[24] ZHONG Li-ping, WANG Yong-jian. Microstructure evolution and optimum parameters analysis for hot working of new type Mg−8Sn−2Zn−0.5Cu alloy [J]. Transactions of Nonferrous Metals Society of China, 2019, 29: 2290−2299.

[25] LIU Hong-mei, CHEN Yun-gui, TANG Yong-bai, WEI Shang-hai, NIU Gao. The microstructure, tensile properties, and creep behavior of as-cast Mg−(1−10)%Sn alloys [J]. Journal of Alloys and Compounds, 2007, 440: 122−126.

[26] SONG Guang-ling, XU Zhen-qing. Effect of microstructure evolution on corrosion of different crystal surfaces of AZ31 Mg alloy in a chloride containing solution [J]. Corrosion Science, 2012, 54: 97−105.

[27] SONG Guang-ling, ATRENS A. Understanding magnesium corrosion—A framework for improved alloy performance [J]. Advanced Engineering Materials, 2003, 5: 837−858.

[28] GUI Zhen-zhen, KANG Zhi-xin, LI Yuan-yuan. Corrosion mechanism of the as-cast and as-extruded biodegradable Mg−3.0Gd−2.7Zn−0.4Zr−0.1Mn alloys [J]. Materials Science and Engineering C, 2019, 96: 831−840.

[29] ZHANG Xiao-bo, WANG Zhang-zhong, YUAN Guang-yin, XUE Ya-jun. Improvement of mechanical properties and corrosion resistance of biodegradable Mg−Nd−Zn−Zr alloys by double extrusion [J]. Materials Science and Engineering B, 2012, 177: 1113−1119.

[30] KIM H S, KIM G H, KIM H, KIM W J. Enhanced corrosion resistance of high strength Mg−3Al−1Zn alloy sheets with ultrafine grains in a phosphate-buffered saline solution [J]. Corrosion Science, 2013, 74: 139−148.

[31] HAN G, LEE J Y, KIM Y C, PARK J H, KIM D I, HAN H S, YANG S J, SEOK H K. Preferred crystallographic pitting corrosion of pure magnesium in Hanks' solution [J]. Corrosion Science, 2012, 63: 316−322.

[32] CHENG Yuan-fen, DU Wen-bo, LIU Ke, FU Jun-jian, WANG Zhao-hui, LI Shu-bo, FU Jin-long. Mechanical properties and corrosion behaviors of Mg−4Zn−0.2Mn−0.2Ca alloy after long term in vitro degradation [J]. Transactions of Nonferrous Metals Society of China, 2020, 30: 363−372.

[33] XU Yu-zhao, LI Jing-yuan, QI Ming-fan, GU Jin-bo, ZHANG Yuan. Effect of extrusion on the microstructure and corrosion behaviors of biodegradable Mg−Zn−Y−Gd−Zr alloy [J]. Journal of Materials Science, 2019, 55: 1231−1245.

[34] ORLOV D, RALSTON K D, BIRBILIS N, ESTRIN Y. Enhanced corrosion resistance of Mg alloy ZK60 after processing by integrated extrusion and equal channel angular pressing [J]. Acta Materialia, 2011, 59: 6176−6186.

[35] SONG Guang-ling, XU Zhen-qing. Crystal orientation and electrochemical corrosion of polycrystalline Mg [J]. Corrosion Science, 2012, 63: 100−112.

[36] SONG Guang-ling, MISHRA R, XU Zhen-qing. Crystallographic orientation and electrochemical activity of AZ31 Mg alloy [J]. Electrochemistry Communications, 2010, 12: 1009−1012.

[37] MCCALL C R, HILL M A, LILLARD R S. Crystallographic pitting in magnesium single crystals [J]. Corrosion Engineering, Science and Technology, 2013, 40: 337−343.

[38] MIAO Hong-wei, HUANG Hua, SHI Yong-juan, ZHANG Hua, PEI Jia, YUAN Guang-yin. Effects of solution treatment before extrusion on the microstructure, mechanical properties and corrosion of Mg−Zn−Gd alloy in vitro [J]. Corrosion Science, 2017, 122: 90−99.

[39] CHANG Jian-wei, GUO Xing-wu, FU Peng-huai, PENG Li-ming, DING Wen-jiang. Effect of heat treatment on corrosion and electrochemical behaviour of Mg−3Nd−0.2Zn−0.4Zr (wt.%) alloy [J]. Electrochimica Acta, 2007, 52: 3160−3167.

[40] LIU Yang, WU Yuan-hao, BIAN Dong, GAO Shuang, LEEFLANG S, GUO Hui, ZHENG Yu-feng. Study on the Mg−Li−Zn ternary alloy system with improved mechanical properties, good degradation performance and different responses to cells [J]. Acta Biomaterialia, 2017, 62: 418−433.

[41] WANG Wei-dan, HAN Jun-jie, YANG Xuan, LI Mei, WAN Peng, TAN Li-li, ZHANG Yu, YANG Ke. Novel biocompatible magnesium alloys design with nutrient alloying elements Si, Ca and Sr: Structure and properties characterization [J]. Materials Science and Engineering B, 2016, 214: 26−36.

显微组织特征对 Mg–5Sn–3In 合金在 Hank's 溶液中腐蚀行为的影响

王雪健[1]，陈宗宁[1,2]，张瑜博[3]，郭恩宇[1,2]，康慧君[1,2]，韩 培[3]，王同敏[1,2]

1. 大连理工大学 材料科学与工程学院 凝固控制与数字化制备技术辽宁省重点实验室，大连 116024；
2. 大连理工大学 宁波研究院，宁波 315000；
3. 上海交通大学 附属第六人民医院 骨科，上海 200233

摘 要：通过显微组织观察、失重实验、动态极化曲线测试和腐蚀形貌表征等手段研究挤压后显微组织的改变对 Mg−5Sn−3In 合金在 Hank's 溶液中腐蚀行为的影响。结果表明：挤压后合金的腐蚀速率与铸态合金相似，但是挤压加工极大地降低了合金局部腐蚀敏感性，特别是沿着挤压方向。挤压态合金相对均匀的腐蚀形貌主要归功于合金中细小均匀分布的 Mg_2Sn 颗粒和显著的结晶取向。同时，细胞毒性实验证明 Mg–5Sn–3In 合金对 NIH3T3 细胞毒性检测等级为 0~1 级，表明合金对 NIH3T3 细胞呈现无毒性。

关键词：Mg–Sn 合金；铟元素；显微组织；腐蚀行为；细胞毒性

(Edited by Wei-ping CHEN)